Strong long-wave infrared optical response in a topological semiconductor with a Mexican-hat band structure

Mark J. Polking [1,*] Haowei Xu [2] Raman Sankar,[3] Kevin Grossklaus [4] and Ju Li [2,5,†]

[1]*Advanced Materials and Microsystems Group, Massachusetts Institute of Technology Lincoln Laboratory, Lexington, Massachusetts 02421, USA*

[2]*Department of Nuclear Science and Engineering, Massachusetts Institute of Technology, Cambridge, Massachusetts 02139, USA*

[3]*Institute of Physics, Academia Sinica, Taipei 11529, Taiwan*

[4]*Department of Electrical and Computer Engineering, Tufts University, Medford, Massachusetts 02155, USA*

[5]*Department of Materials Science and Engineering, Massachusetts Institute of Technology, Cambridge, Massachusetts 02139, USA*

(Received 21 October 2024; revised 20 December 2024; accepted 8 January 2025; published 3 February 2025)

Light sources and photodetectors operating in the far- to midinfrared (FIR/MIR) band (8–12 μm, 0.15–0.1 eV) remain relatively poorly developed compared to their counterparts operating in the visible and near-infrared ranges, despite extensive application potential for thermal imaging, standoff sensing, and other technologies. This is attributable in part to the lack of narrow-gap materials (<0.1 eV) with high optical gain and absorption. In this work, a narrow-gap semiconductor, $Pb_{0.7}Sn_{0.3}Se$, is demonstrated to exhibit an optical response >10× larger than that of $Hg_xCd_{1-x}Te$ (MCT), the dominant material for FIR/MIR photodetectors. A previous theoretical investigation indicated that chalcogen *p* and metal *d* band inversion in this material creates a Mexican hat band structure (MHBS), which results in a dramatic increase in the joint density of states at the optical transition edge compared to typical semiconductors. This prediction is experimentally validated here using single-crystal specimens of $Pb_{0.7}Sn_{0.3}Se$ measured using temperature-dependent spectroscopic ellipsometry over a wavelength range 1.7–20 μm (0.73–0.062 eV). These measurements demonstrate a large enhancement in extinction coefficient and refractive index, which are characteristic of a MHBS in the vicinity of the absorption edge, in agreement with theoretical predictions. The realization of topological semiconductors with a MHBS is expected to lead to high-efficiency detectors operating in the FIR/MIR range.

DOI: 10.1103/PhysRevB.111.085101

I. INTRODUCTION

The far- to midinfrared (FIR/MIR) portion of the electromagnetic spectrum spanning the 8–12-micron (0.15–0.1 eV) wavelength band is of increasing importance for thermal imaging [1], chemical sensing [2–4], hyperspectral imaging [5], and numerous other critical application areas. Despite the expanding application space of the FIR/MIR, however, technological progress in this spectral range continues to be outpaced by the rapid advances in the visible, near-IR (NIR), and MIR bands, in part due to a dearth of high-efficiency sources and detectors with low fabrication cost and high fabrication yield [6,7]. Rapid progress in the visible-MIR portion of the spectrum has been facilitated by the widespread availability of efficient, low-cost photodiode detectors and diode laser sources, which can be fabricated at scale from highly mature III-V and group IV semiconductors [8]. FIR/MIR systems, in contrast, have long relied on detectors based on the ternary semiconductor $Hg_xCd_{1-x}Te$ (MCT), which suffers from poor fabrication yield and poor optical absorption [9], and on quantum cascade laser (QCL) sources, which are limited by similarly high fabrication costs, low power output, and low efficiencies [6,7].

A promising solution to this paucity of suitable FIR/MIR source and detector technologies is the development of narrow-gap semiconductor systems with enhanced optical absorption/gain, high defect tolerance, and crystal structures amenable to monolithic integration on established III-V and group IV semiconductor platforms. Recently, several of the authors predicted a large enhancement in optical absorption and gain near the band edge in narrow-gap topological semiconductors with strong band inversion, characterized by a reversal of the typical energy ordering of the metal *d* states and the chalcogen *p* states in some regions of the $\boldsymbol{k}$ space [10]. These materials exhibit narrow, direct band gaps induced by spin-orbit coupling with a typical magnitude of under 0.1 eV as well as a so-called "Mexican hat" band structure, illustrated schematically in Fig. 1. The band topology of these materials results in a large enhancement of the joint density of states (JDOS) at the band edge, leading to an enhancement of optical absorption/gain by 1–2 orders of magnitude compared to semiconductors with conventional parabolic bands, such as MCT. The direct band gaps and strong optical responses in these materials provide an ideal combination of properties for achieving improved performance of FIR/MIR optical devices.

In this work, we experimentally demonstrate strong optical absorption in an alloy of two of these predicted materials,

*Contact author: mark.polking@ll.mit.edu
†Contact author: liju@mit.edu

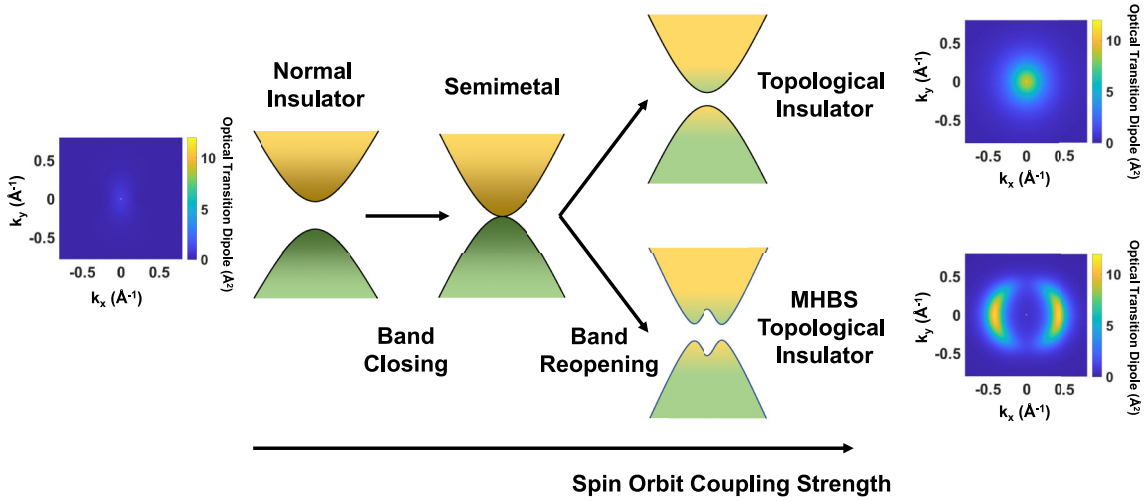

FIG. 1. Emergence of a Mexican hat band structure (MHBS) with increasing spin-orbit coupling strength in a narrow-gap topological semiconductor. The optical transition matrix element and joint density of states are greatly enhanced in a topological semiconductor with a MHBS (lower right) compared to topological semiconductors with parabolic band structure (upper right) and normal semiconductors (left). The optical transition dipole is defined as $|\langle ck|r|vk\rangle|^2$, where r is the position operator, while $|ck\rangle$ and $|vk\rangle$ are the conduction and valence band wave functions, respectively. Adapted from Ref. [10]. Note that these materials are typically referred to as topological insulators, although their bandgaps are generally below 0.5 eV. In this work, we use the term "topological semiconductor" to align with the nomenclature commonly adopted in the semiconductor community.

SnSe and PbSe, stabilized in the rocksalt crystal structure predicted to yield a Mexican hat band structure (MHBS). This material system was chosen due to the ability to continuously tune the optical band gap over a wide range with material stoichiometry [11], and the ample heritage of lead salts in diode lasers systems and low-cost infrared detectors dating back to the 1960s [12]. High-quality single-crystal specimens of material with a composition of $Pb_{0.7}Sn_{0.3}Se$ were grown via the Bridgman method and characterized with temperature-dependent infrared spectroscopic ellipsometry. These measurements demonstrate an absorption coefficient as large as $2.0 \times 10^4\,cm^{-1}$ at a wavelength of 12 μm, an enhancement of $>10\times$ compared to the band edge absorption of typical MCT samples with a CdTe mole fraction of 0.2 suitable for operation in the FIR/MIR [13]. Optical constants measured as functions of frequency and temperature with ellipsometry are in good agreement with predictions generated with linear response theory for varying values of carrier scattering lifetimes and prior predictions of Xu *et al.* [10]. In addition to exceptional optical responses, this material also possesses a very large static dielectric constant (∼200) [14]. High dielectric constants in similar lead chalcogenide materials have been shown to yield far superior defect tolerance compared with III-V materials and MCT [15], potentially enabling greatly improved device fabrication yield. In addition, the lattice constant of this material system enables direct monolithic heteroepitaxial integration on common III-V semiconductor substrates [16] and epitaxial integration on Si-Ge using alkaline-earth halide buffer layers, as demonstrated for similar lead chalcogenides in prior reports [17,18]. This combination of narrow, compositionally tunable band gaps, exceptional optical responses, high defect tolerance, and compatibility with mature semiconductor platforms provides an ideal starting point for next-generation FIR/MIR sources and detectors.

II. RESULTS

As predicted previously by Xu *et al.*, both PbSe and SnSe in the rocksalt phase exhibit a MHBS, suggesting that ternary alloys could provide a material system with a composition tunable band gap. Bulk SnSe, however, exists in an orthorhombic crystal structure derived from the higher symmetry rocksalt structure by a small cell-doubling displacive transition [19]. A prior study indicates that SnSe-PbSe alloys must consist of at least 67% PbSe to achieve a single-phase material in the rocksalt structure, which is stable for all compositions up to pure PbSe, and thus $Pb_{0.7}Sn_{0.3}Se$ was selected as a starting composition [20]. Single crystals of $Pb_{0.7}Sn_{0.3}Se$ were prepared from high-purity Sn, Se, and Pb feedstocks using a two-stage vertical Bridgman growth process. Further details are provided in Ref. [21], and images of typical crystal pieces are shown in Fig. S1 in Ref. [21]. Analysis of pulverized material with x-ray diffraction demonstrates single-phase material in the cubic rocksalt structure, as illustrated in Fig. 2(a). Application of the extrapolation procedure of Nelson and Riley yields a cubic lattice constant of 6.0908 Å, reduced from the value of 6.12 Å for pure PbSe as expected [22,23]. Elemental analysis with energy-dispersive x-ray spectroscopy (EDS) in a scanning electron microscope [Fig. 2(b)] demonstrates a composition of $(Pb_{0.74}Sb_{0.26})Se_{0.97}$, very close to the target composition within the typical error of EDS.

Pieces of the bulk crystal were analyzed using infrared spectroscopic ellipsometry over a wavelength range 1.7–20 μm (0.73–0.062 eV). Measurements were performed using a JA Woollam IR-VASE Mark II spectroscopic ellipsometer equipped with a broadband SiC globar source. The IR-VASE enables high-resolution measurements over a wavelength range 1.7–30 μm, but the measurement range in this experiment was limited to 1.7–20 μm due to the limited transmission range of the ZnSe windows. The effects of the ZnSe windows

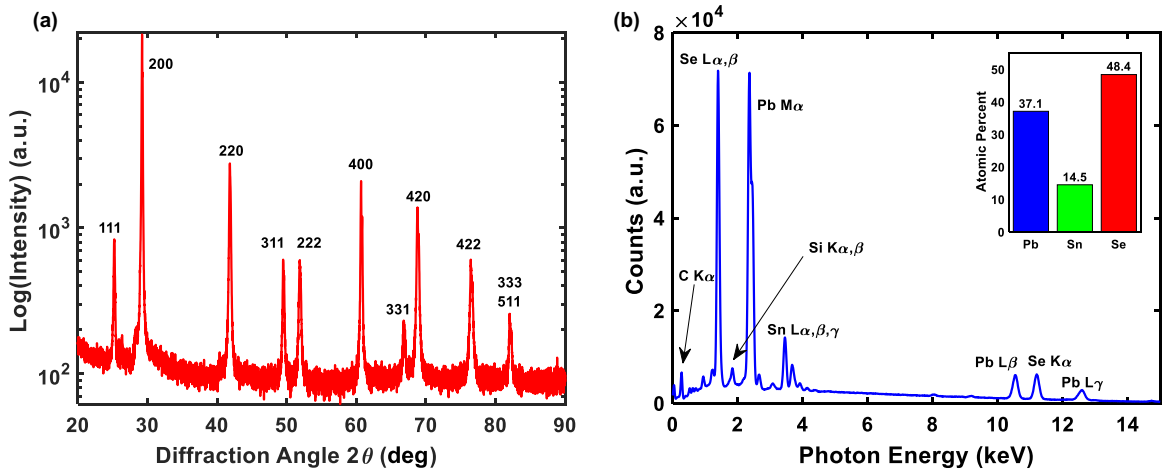

FIG. 2. Structural and chemical characterization of a sample with a nominal composition of $Pb_{0.7}Sn_{0.3}Se$. (a) X-ray diffraction scan of a pulverized single crystal of cubic-phase $Pb_{0.7}Sn_{0.3}Se$ grown by the Bridgman technique. All diffraction peaks can be assigned to the cubic rocksalt structure expected for $Pb_{0.7}Sn_{0.3}Se$. (b) Energy-dispersive x-ray spectroscopy (EDS) analysis of the stoichiometry of a $Pb_{0.7}Sn_{0.3}Se$ specimen. The measured composition matches the nominal target composition within the typical error of EDS.

on the ellipsometry measurement were accounted for using a JA Woollam proprietary calibration method prior to measurement. Due to the construction of the cryostat, the angle of incidence was fixed at 70°. Samples were scanned with a fixed polarizer angle of 45° and a resolution of 16 cm^{-1}. Prior to measurement, the crystal pieces were mechanically polished along (100) planes and mounted on roughened Si substrates to suppress depolarization effects due to diffuse surface reflections and back surface reflections, respectively (Fig. S2 in Ref. [21]). The extinction coefficient κ and refractive index n of $Pb_{0.7}Sn_{0.3}Se$ samples were measured in a cryostat under high vacuum at temperatures from 77 K up to ambient temperature (Fig. 3). For the purposes of calculating n and κ from the ellipsometric measurement data, the sample was treated as a single, homogeneous layer. Measurements of the extinction coefficient demonstrate a marked enhancement from 270 to 77 K in the vicinity of the band edge with a peak value of approximately 1.75 at an energy of 0.1 eV. The sharp peak observed is consistent with the predictions of Xu *et al.* for rocksalt SnSe with a MHBS [10]. This peak is a characteristic of MHBS as conventional semiconductors with parabolic band structure should exhibit

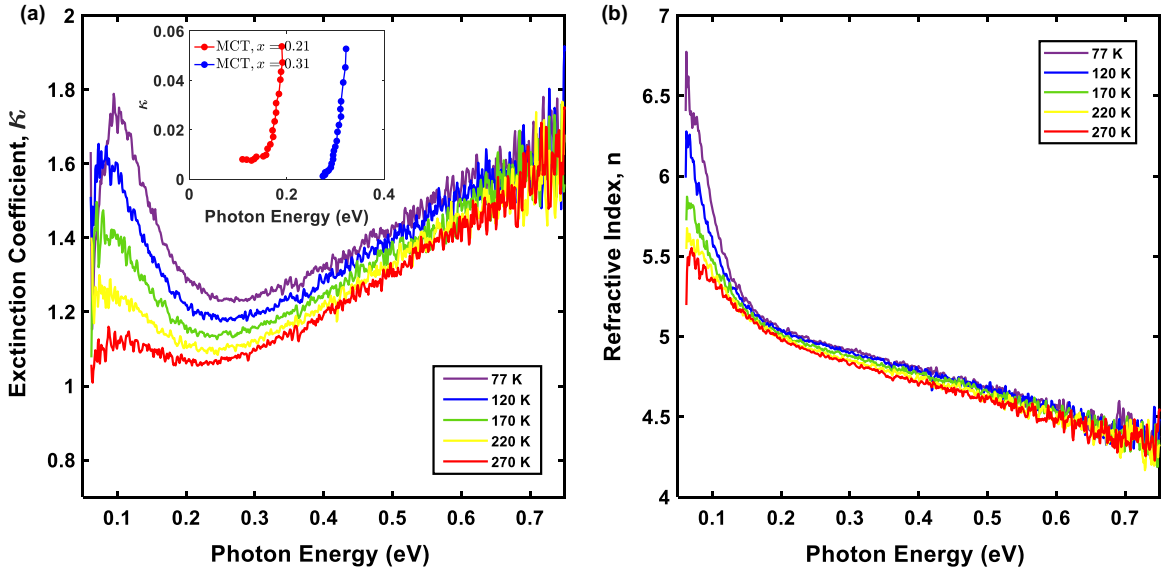

FIG. 3. Temperature-dependent spectroscopic ellipsometry measurements of a rocksalt $Pb_{0.7}Sn_{0.3}Se$ single crystal specimen from 77 to 270 K illustrating an optical response characteristic of a Mexican hat band structure (MHBS). (a) Extinction coefficient as a function of photon energy, and (b) real part of the refractive index as a function of photon energy. Large enhancements of both the real and imaginary parts of the refractive index can be observed near the band edge. Particularly, there is a sharp peak in κ near the band edge. This should be compared with semiconductors with conventional parabolic band structure, where κ would increase monotonically but slowly near the band edge. This is consistent with prior predictions of the optical response of a topological semiconductor with a MHBS [10] [cf. Fig. 4(a)], and is a characteristic of MHBS. Inst of (a) shows the extinction coefficient κ of $Hg_xCd_{1-x}Te$ (MCT), which are adapted from Ref. [24].

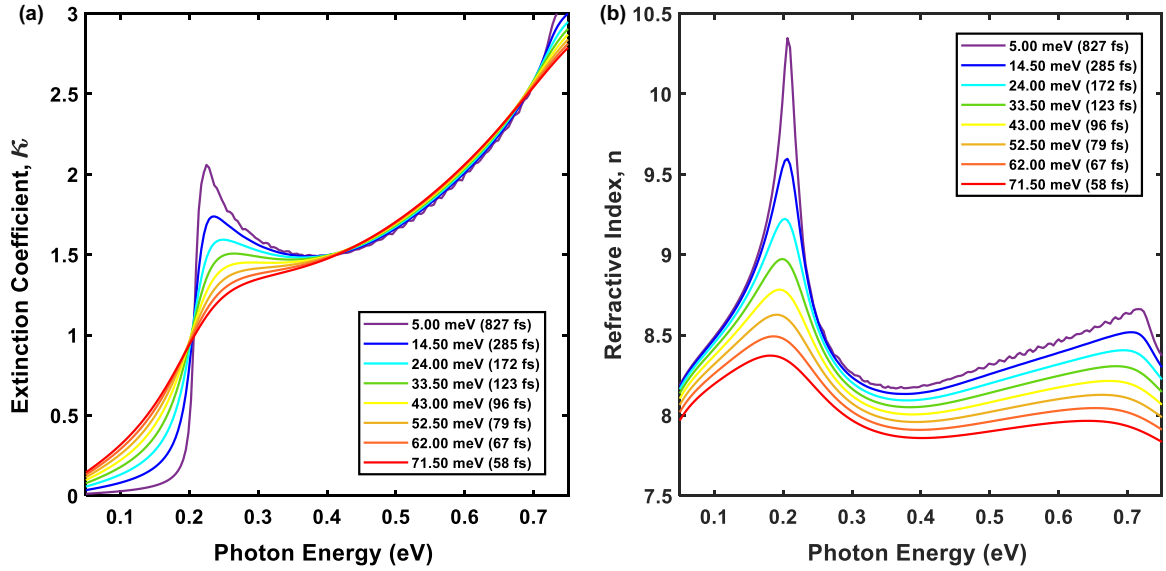

FIG. 4. Simulated optical constants of SnSe in the rocksalt structure for varying carrier scattering times. (a) Extinction coefficient vs photon energy, and (b) the real part of the refractive index vs photon energy. The predicted behavior of both the real and imaginary parts of the refractive index is in close agreement with the experimental measurements shown in Fig. 3. The color of the line indicates the electron linewidth (lifetime) used in Eq. (1).

κ that increase monotonically but slowly near the band edge. Measurements of the real part of the refractive index also show a large enhancement from 270 to 77 K, reaching a peak value of 6.5 at the latter temperature. Particulalry, the extinction coefficient κ is larger than that of MCT by more than ten times in the same frequency range [inset of Fig. 3(a)]. The measurements show low levels of depolarization (Fig. S3 in Ref. [21]), indicating low levels of diffuse surface scattering and back-surface reflections. We also calculated the peak value of the imaginary part of the dielectric constant $\varepsilon^{(2)}$ of $Pb_{0.7}Sn_{0.3}Se$ from the measured values for n and κ, which yields $\varepsilon^{(2)} \approx 22$. This is far larger than values predicted by Xu *et al.* for SnSe under 8% tensile strain, which is topologically trivial without band inversion (typically $\varepsilon^{(2)} < 3$ near the band edge). Meanwhile, the measured $\varepsilon^{(2)}$ of $Pb_{0.7}Sn_{0.3}Se$ is still smaller than the predicted value for unstrained SnSe by Xu *et al.* (roughly 60), which is topologically nontrivial with MBHS. This may be attributable to alloying with PbSe, which is predicted to exhibit an optical gain that is ∼35% smaller than the value predicted for pure SnSe ($2.6 \times 10^4\,\mathrm{cm}^{-1}$ vs $4.0 \times 10^4\,\mathrm{cm}^{-1}$) in the rocksalt phase. Also, the calculations by Xu *et al.* assumed zero temperature and an electron relaxation time of 0.8 ps. At finite temperature with potentially shorter electron relaxation time, which is relevant to our experiments, the peak of $\varepsilon^{(2)}$ would be lower [cf. Fig. 4(b)].

The temperature dependencies of the optical constants observed here are inconsistent with thermorefractive effects common to semiconductors. A large enhancement of the refractive index is observed only within ∼0.1 eV of the band edge, suggesting that thermorefractive effects common to semiconductors are not responsible for the observed behavior. The increase in refractive index of ∼0.1 observed at higher energies upon cooling from 270 to 77 K is consistent with prior measurements of pure PbSe, which exhibits negative thermorefraction [18]. An increase in free carrier absorption can also be excluded as a source of this temperature dependence. Increasing free carrier absorption results in an increase in the extinction coefficient, but a coincident decrease in the real part of the refractive index, in stark contrast to our results showing marked increases in both quantities with decreasing temperature. The sharp absorption peak observed is also inconsistent with the typical $1/f^2$ dependence of free carrier absorption according to the Drude model [25].

To better understand the experimental results and elucidate the origin of the temperature dependence, we performed first-principles calculations of the linear optical responses (details in Ref. [21]). Due to the high computation cost for simulations of $Pb_{0.7}Sn_{0.3}Se$ alloys, we used SnSe as a test case to illustrate the behavior of the optical response of a MHBS topological insulator near the band edge and its temperature dependence. Specifically, we first calculated the dielectric response function using the linear response theory, which can be expressed as

$$\varepsilon_{pq}(\omega) = \delta_{pq} - \frac{e^2}{\varepsilon_0} \int \frac{d^3\boldsymbol{k}}{(2\pi)^3} \sum_{m,n} \frac{(f_m - f_n)\langle m|r^p|n\rangle\langle n|r^q|m\rangle}{E_n - E_m - \hbar\omega - i\eta}, \tag{1}$$

where $r^{p,q}$ is the position operator with Cartesian indices p and q. δ_{pq} is the Kronecker delta, ε_0 is the vacuum permittivity, and f_m and E_m are the occupation number and energy of the electronic state $|m\rangle$, respectively. The dependence on electron wave vector $\boldsymbol{k}$ is omitted for simplicity. The parameter $\eta = \frac{1}{\tau}$ is the linewidth of the electrons, and τ is the carrier relaxation time. Here we assume τ is a constant for all electrons (constant relaxation time approximation). Then, the extinction coefficient κ and refractive index n can be obtained from the equation:

$$n(\omega) + i\kappa(\omega) = \sqrt{\varepsilon(\omega)}. \tag{2}$$

It should be noted that in a perfect crystal, changes in temperature primarily result in two consequences. First, the occupation number f_m follows the Fermi-Dirac distribution. The band gap of SnSe ($Pb_{0.7}Sn_{0.3}Se$) is around 0.1 eV, equivalent to over 1000 K. Hence, the temperature variance between 77 and 270 K does not lead to a significant change in f_m. On the other hand, temperature variations can also affect the carrier scattering time τ, which is typically substantially reduced at elevated temperatures [26,27]. Since it is not straightforward to predict τ as a function of temperature, especially for alloy systems, we manually vary τ and calculate $n(\omega)$ and $\kappa(\omega)$ for different τ values. The results are shown in Fig. 4. Similar to the experimental results, peaks in both $n(\omega)$ and $\kappa(\omega)$ are clearly observable when ω is close to the band edge (around 0.2 eV for SnSe in the rocksalt phase in our calculations, not 0.1 eV as in experiments). These peaks come from the fast electronic interband transitions near the band edge and are a characteristic feature of topological semiconductors with a MHBS, which leads to a large JDOS. As shown in our simulations, when τ becomes shorter, corresponding to a higher temperature, the peaks in n and κ become less prominent, consistent with experimental results as well. This reduction in peak magnitude for shorter values of τ (larger η) is due to the smearing of the topological electronic states near the band edge.

III. CONCLUSIONS

Our results demonstrate the feasibility of achieving a large enhancement of optical responses in the FIR/MIR spectral region due to ample d-p orbital character mixing arising from topological band inversion, and a special Mexican hat band structure in the rocksalt phase of PbSe-SnSe alloys, consistent with prior theoretical studies. The direct band gap in this class of TI is proportional to the spin-orbit coupling strength, which has a suitable magnitude for FIR/MIR devices. Our measurements of the optical constants of high-quality single crystals of the topological semiconductor $Pb_{0.7}Sn_{0.3}Se$ with spectroscopic ellipsometry clearly demonstrate a pronounced absorption peak near the band edge and coincident enhancement of the refractive index, arising from (a) an inordinately large d-p mixing due to the topological band inversion across the direct band gap, which enhances the optical transition matrix element, and (b) the high JDOS of a MHBS material, for which the optical transition can occur on a ring of degenerate states rather than at a single $\boldsymbol{k}$ point in the Brillouin zone, as for a standard topological semiconductor without a MHBS (Fig. 1). The temperature dependence of the optical constants closely matches the results of first-principles calculations of the temperature-dependent optical response of a MHBS semiconductor with free carriers derived from linear response theory.

This work highlights a pathway to the engineering of large optical responses in materials with band gaps suitable for the underdeveloped FIR/MIR spectral range. As shown previously [10], numerous other material systems are predicted to exhibit a similar MHBS associated with strong optical responses. Further development of these materials is anticipated to enable next-generation light sources and photodetectors with improved optical gain and detection efficiency, respectively, with broad applications to thermal imaging, standoff chemical sensing, hyperspectral imagers, and beyond.

ACKNOWLEDGMENTS

M.J.P. acknowledges M. Walsh for assistance with optical polishing of specimens. R.S. acknowledges the financial support provided by the Ministry of Science and Technology in Taiwan under Projects No. NSTC-113-2124-M-001-003 and No. NSTC-113-2112M001-045-MY3, as well as support from Academia Sinica for the budget of AS-iMATE11412. J.L. and H.-W.X. acknowledge support by Office of Naval Research Multidisciplinary University Research Initiative Award No. ONR N00014-18-1-2497. The calculations in this work were performed in part on the Texas Advanced Computing Center (TACC) and MIT Engaging Cluster. Ellipsometry measurements were performed at the Tufts Epitaxial Core Facility.

The authors declare no conflicts of interest.

DATA AVAILABILITY

The data that support the findings of this study are available from the corresponding authors upon reasonable request.

[1] T. X. B. Nguyen, K. Rosser, and J. Chahl, A review of modern thermal imaging sensor technology and applications for autonomous aerial navigation, J. Imaging **7**, 217 (2021).

[2] M. C. Phillips, B. E. Bernacki, P. T. Conry, and M. J. Brown, Standoff infrared measurements of chemical plume dynamics in complex terrain using a combination of active swept-ECQCL laser spectroscopy with passive hyperspectral imaging, Remote. Sens. **14**, 3756 (2022).

[3] J. A. Seeley and J. M. Richardson, Early Warning Chemical Sensing, Lincoln Laboratory J. **17**, 85 (2007).

[4] P. Wen, M. Amin, W. D. Herzog, and R. R. Kunz, Key challenges and prospects for optical standoff trace detection of explosives, TrAC Trends Anal. Chem. **100**, 136 (2018).

[5] D. Manolakis, M. Pieper, E. Truslow, R. Lockwood, A. Weisner, J. Jacobson, and T. Cooley, Longwave infrared hyperspectral imaging: Principles, progress, and challenges, IEEE Geosci. Remote Sens. Mag. **7**, 72 (2019).

[6] Y. Yao, A. J. Hoffman, and C. F. Gmachl, Mid-infrared quantum cascade lasers, Nat. Photon. **6**, 432 (2012).

[7] M. S. Vitiello, G. Scalari, B. Williams, and P. De Natale, Quantum cascade lasers: 20 years of challenges, Opt. Express **23**, 5167 (2015).

[8] W. N. Ye and Y. Xiong, Review of silicon photonics: History and recent advances, J. Mod. Opt. **60**, 1299 (2013).

[9] W. Lei, J. Antoszewski, and L. Faraone, Progress, challenges, and opportunities for HgCdTe infrared materials and detectors, Appl. Phys. Rev. **2**, 041303 (2015).

[10] H. Xu, J. Zhou, H. Wang, and J. Li, Giant photonic response of mexican-hat topological semiconductors for mid-infrared

to terahertz applications, J. Phys. Chem. Lett. **11**, 6119 (2020).
[11] H. Preier, Physics and applications of IV-VI compound semiconductor lasers, Semicond. Sci. Technol. **5**, S12 (1990).
[12] H. Preier, Recent advances in lead-chalcogenide diode lasers, Appl. Phys. **20**, 189 (1979).
[13] J. Chu, Z. Mi, and D. Tang, Band-to-band optical absorption in narrow-gap $Hg_{1-x}Cd_xTe$ semiconductors, J. Appl. Phys. **71**, 3955 (1992).
[14] M. Tacke and Lead–salt lasers, Philos. Trans. R. Soc. London, Ser. A **359**, 547 (2001).
[15] S. L. Elizondo, F. Zhao, J. Kar, J. Ma, J. Smart, D. Li, S. Mukherjee, and Z. Shi, Dielectric charge screening of dislocations and ionized impurities in PbSe and MCT, J. Elect. Mater. **37**, 1411 (2008).
[16] J. Meyer, A. J. Muhowski, L. Nordin, E. Hughes, B. Haidet, D. Wasserman, and K. Mukherjee, Bright mid-infrared photoluminescence from high dislocation density epitaxial PbSe films on GaAs, APL Mater. **9**, 111112 (2021).
[17] A. Belenchuk, A. Fedorov, H. Huhtinen, V. Kantser, R. Laiho, O. Shapoval, and V. Zakhvalinskii, Growth of (111)-oriented PbTe ®lms on Si(001) using a BaF_2 buffer, Thin Solid Films **358**, 277 (2000).
[18] H. Zogg and M. Hüppi, Growth of high quality epitaxial PbSe onto Si using a $(Ca, Ba)F_2$ buffer layer, Appl. Phys. Lett. **47**, 133 (1985).
[19] G. S. Pawley, Evidence for ferroelectricity in IV-VI compounds, J. Phys. Colloq. **29**, C4 (1968).
[20] H. Krebs and D. Langner, Über Struktur und Eigenschaften der Halbmetalle. XVI. Mischkristallsysteme zwischen halbleitenden Chalkogeniden der vierten Hauptgruppe. II, Z. Anorg. Allg. Chem. **334**, 37 (1964).
[21] See Supplemental Material at http://link.aps.org/supplemental/10.1103/PhysRevB.111.085101 for descriptions of the experimental and theoretical methods used in this work.
[22] J. B. Nelson and D. P. Riley, An experimental investigation of extrapolation methods in the derivation of accurate unit-cell dimensions of crystals, Proc. Phys. Soc. **57**, 160 (1945).
[23] A. N. Mariano and K. L. Chopra, Polymorphism in some iv-vi compounds induced by high pressure and thin-film epitaxial growth, Appl. Phys. Lett. **10**, 282 (1967).
[24] M. W. Scott, Energy Gap in $Hg_{1-x}Cd_xTe$ by Optical Absorption, J. Appl. Phys. **40**, 4077 (1969).
[25] Charles Kittel and Paul McEuen, *Introduction to Solid State Physics* (John Wiley and Sons, New York, 2018).
[26] F. Ichihashi, T. Kawaguchi, X. Dong, M. Kuwahara, T. Ito, S. Harada, M. Tagawa, and T. Ujihara, Temperature dependence of carrier relaxation time in gallium phosphide evaluated by photoemission measurements, AIP Adv. **7**, 115314 (2017).
[27] H. H. Hegazy, Semiconducting chalcogenide Ge-Se-Sb-Cu as new prospective thermoelectric materials, Res. Phys. **14**, 102492 (2019).

Supporting Information for:

Giant Long-Wave Infrared Optical Response in a Topological Semiconductor with a Mexican Hat Band Structure

Mark J. Polking, Haowei Xu, Raman Sankar, Kevin Grossklaus, and Ju Li

Synthesis of $Pb_{0.7}Sn_{0.3}Se$ Single Crystals:

High-quality single crystals of $Pb_{0.7}Sn_{0.3}Se$ were obtained using a vertical Bridgman growth process. The process involved two stages in order to control the severe Se vapor loss and maintain the expected Pb:Sn ratio. In the first stage, bulk $Pb_{1-x}Sn_xSe$ crystals were prepared by a conventional melt growth approach. Stoichiometric amounts of Pb, Sn and Se powders with purities of at least 99.999% were mixed and loaded into a quartz ampoule in an argon-filled glove box. The ampoule was sealed after being evacuated to about 3×10^{-4} Torr. The sealed ampoule was then slowly heated to 850 °C and held at this temperature for 24 hours. The furnace was slowly cooled down to 600 °C at a cooling rate of 5 °C per minute, followed by furnace cooling to room temperature. The crystals obtained from this first growth stage were subsequently ground into powders as the source material for a second Bridgman growth process. In the second stage, each $Pb_{1-x}Sn_xSe$ pre-reacted powder sample (~10 grams) was carefully placed in the quartz ampoule and sealed under vacuum. The sealed ampoule was placed inside a two-zone vertical Bridgman furnace with a temperature gradient of (1 °C/cm) within 60 cm. The Bridgman growth process was carried out by keeping the upper zone at 900 °C and the lower zone at 725 °C for 20 days. The ampoules were lowered through a temperature gradient of 1°C/cm at a rate of 0.1 mm/h to obtain a large-size single crystal.

Temperature-Dependent Spectroscopic Ellipsometry Measurements:

A piece of $Pb_{0.7}Sn_{0.3}Se$ single crystal measuring approximately 7 x 5 x 4 mm was first mechanically polished on a (100) face to a mirror finish. The opposite surface was left unpolished and visibly rough to prevent reflections from the back surface. The sample was mounted using colloidal silver paint to a piece of silicon wafer that was mechanically roughened using an alumina particle blaster to reduce reflections. The Si chip was mounted in a Janis Research ST-400 UHV cryostat equipped with ZnSe optical windows and conflat flanges. To prevent ice formation that would impact the measurement results, the cryostat was evacuated to a base pressure of under 5×10^{-9} torr overnight using a pumping station equipped with a turbomolecular pump. The cryostat was then cooled using liquid nitrogen to 77 K for measurements. The sample was heated to temperatures between 77 and 290 K using an internal heater and allowed to stabilize at each temperature for at least five minutes prior to data collection.

Structural and Chemical Characterization:

X-ray diffraction measurements were performed at ambient temperature with Cu K-alpha radiation (λ = 1.5406 Å) using a PANalytical X'Pert Pro powder x-ray diffractometer. Prior to the measurement, a sample of the $Pb_{0.7}Sn_{0.3}Se$ single crystal was ground into a powder using a mortar and pestle. Sample stoichiometry was measured by energy-dispersive x-ray spectroscopy (EDS) using a Zeiss Gemini 500 scanning electron microscope operated at 20 kV and equipped with an Oxford Ultim Max silicon drift EDS detector.

First-Principles Theory Modeling

The density functional theory (DFT)[26,27] calculations in this work were performed using the Vienna *ab initio* simulation package (VASP)[28,29]. The generalized gradient approximation (GGA) in the form of Perdew-Burke-Ernzerhof (PBE)[30] was used to treat the exchange-correlation interactions. The projector augmented wave (PAW) method[31] and a plane wave basis set were used to treat the core and valence electrons, respectively. The first Brillouin zone in the DFT calculations was sampled by a $21 \times 21 \times 21$ $\boldsymbol{k}$-mesh. The Bloch wavefunctions from DFT calculations were used to build a tight-binding (TB) Hamiltonian with the Wannier90 package[32].

The TB Hamiltonian was then used to calculate the dielectric function in Eq. (1) on a much denser $224 \times 224 \times 224$ $\boldsymbol{k}$-mesh.

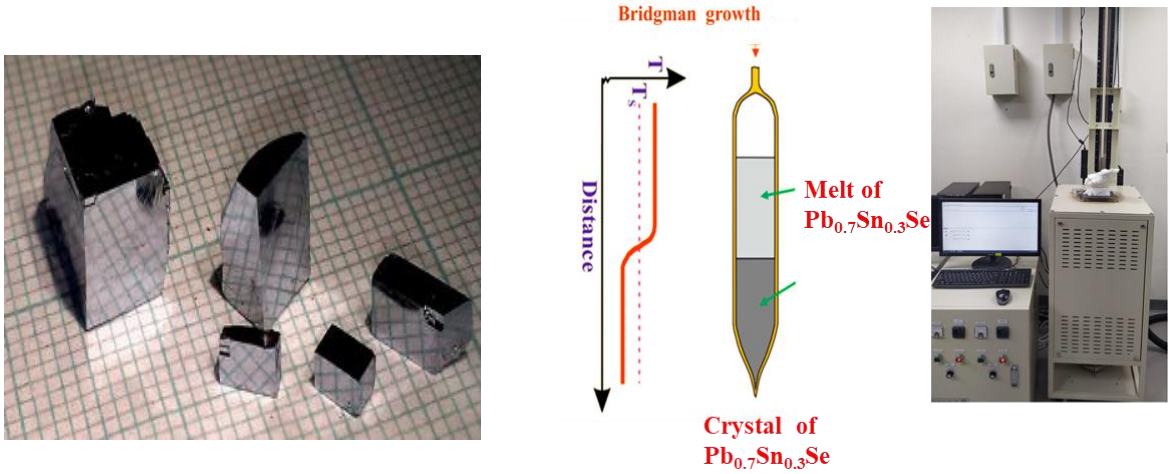

Figure S1. Pieces of the $Pb_{0.7}Sn_{0.3}Se$ single crystal grown by the Bridgman technique.

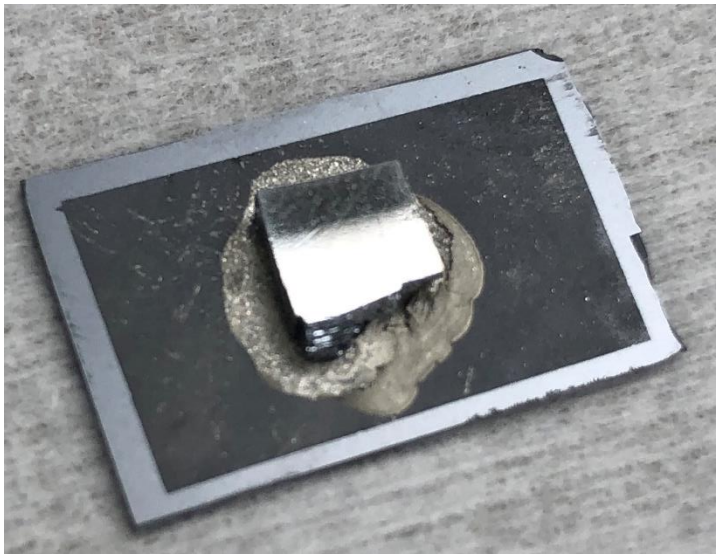

Figure S2. Polished specimen of $Pb_{0.7}Sn_{0.3}Se$ mounted on a roughened Si substrate to suppress back surface reflections during ellipsometric measurement.

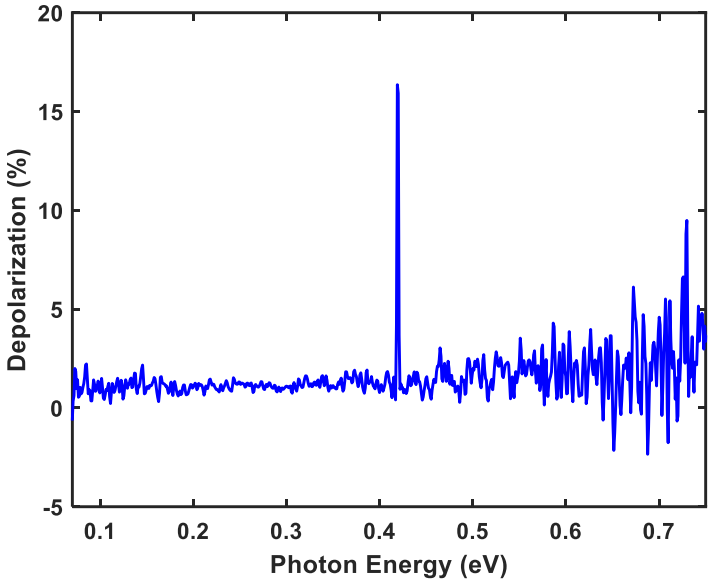

Figure S3. Depolarization vs. photon energy.